10 Particle Physics with CMS

C. Amsler, A. Dorokhov, R. Kaufmann‡, K. Prokofiev, H. Pruys,
C. Regenfus, P. Robmann, T. Speer, and S. Steiner

in collaboration with:
ETH-Zürich, Paul Scherrer Institut (PSI), Universität Basel and the CMS Collaboration.

(CMS Collaboration)

‡ Now at CSEM, Switzerland

10.1 Introduction

We participate in the CMS experiment at the Large Hadron Collider (LHC) where we shall concentrate on physics involving the b-quark, e.g. b-quark production associated with the formation of Higgs bosons, t-quark decays, spectroscopy of B mesons and CP violation in B decays. For a low mass Higgs, below about 135 GeV/^{2}, the dominant decay mode is $H^0 \to b\bar{b}$. The tagging of b-jets is also essential for the detection of the top quark as, V_{tb} being essentially one, the top quark decays nearly exclusively to W^+b. The study of the rare decays $t \to W^+d$ and $t \to W^+s$ gives a direct measurement of the CKM matrix elements V_{td} and V_{ts} and hence, in case unitarity is violated, leads to physics beyond the Standard Model. Also, searches for flavor changing neutral currents in rare B-decays, like B_d or B_s to $\mu^+\mu^-$, are forbidden at the tree level, but may occur at higher orders and therefore allow to test the Standard Model and to probe its extensions at low energy.

The most interesting events at LHC will therefore contain one or several b-jets originating from the decay of B mesons, with typical mean free paths of a few mm. To allow for efficient tagging of B mesons among the large background of light quark and gluon jets, the detection system has to follow particles towards the primary vertex. In fact, our pixel detector, the detector closest to the interaction point, will be located only 4 cm from the beam-beam interaction point. The extremely high particle flux near the primary vertex ($\sim$ 1000 particles every 25 ns, see Fig.10.1) requires the innermost tracking layers to be composed of pixel devices delivering 3D coordinates with high resolution and no ambiguity. Furthermore, the radiation dose to the nearest detector will approach 10^6 Gy (corresponding to 6×10^{14} hadrons /cm^2) after 10 years of LHC operation (Fig.10.2). This is about 10^6 more than for detectors developed earlier for space research.

Our group joined the CMS collaboration in 1995. During the following years we contributed [1, 2, 3] to the development of the pixel detector, the specifications of which are given in the Technical Design Report [4]. We are also responsible for the design and delivery of the mechanical support structure and the service tubes that will transfer the power, the signals and the coolant to the detector. We are participating in the reconstruction and physics simulation software involving the charged particle tracker. In 2000/2001 we initiated a study of various designs for pixel sensors [5] (which will be briefly discussed below) and, recently, we embarked on tests of the readout chips for the pixel sensors.

10.2 The pixel sensors

The CMS pixel detector consists of three cylindrical layers, 53 cm long, with radii of 4.3, 7.1 and 11 cm (Fig. 10.3, and Table 10.1). The barrel layers containing some 3×10^7 silicon pixels

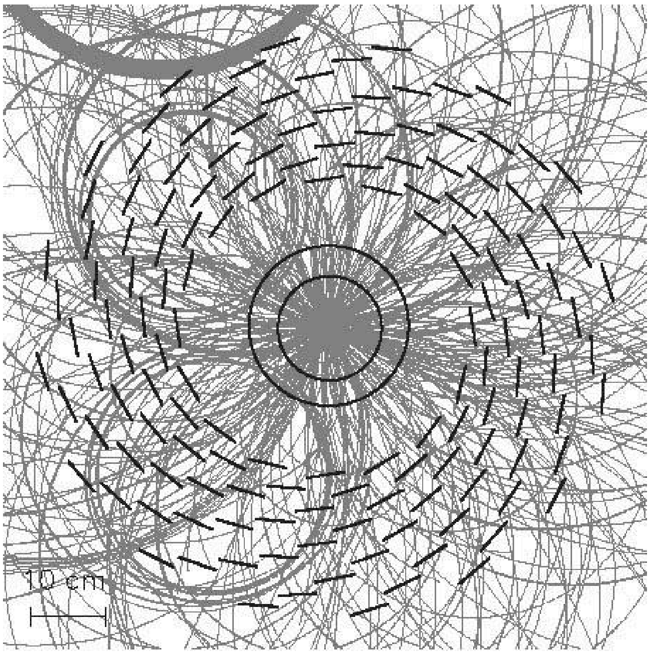

Figure 10.1: *Events of interest will have to be filtered from events with on average 18 superimposed interactions occurring during the same bunch crossing. Shown is a simulated Higgs decay* $H \rightarrow Z^0 Z^0 \rightarrow 2(\mu^+\mu^-)$. *The circles indicate the two innermost pixel layers, the circle segments represent the microstrip silicon tracker.*

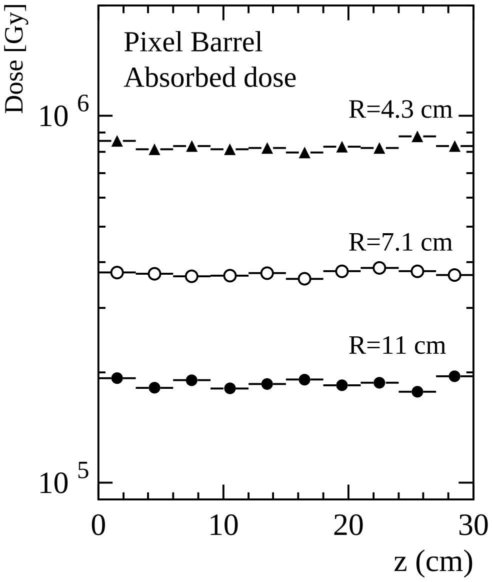

Figure 10.2: *Expected dose absorbed by the CMS pixel barrel in the three layers (radii R), as a function of coordinate along the beam axis (for 10 years of LHC operation).*

will be provided by the ETH-PSI-Basel-Zürich collaboration while the forward/backward wheels will be supplied by the U.S. participants. The pixel modules consist of thin, segmented sensor plates with highly integrated readout chips connected by the indium bump bonding technique (Fig.10.4). A sensor plate contains 53 × 52 pixels, each with an area of 150×150 μm^2 and a thickness of 200 μm. The analog signals are read out to determine the coordinates more accurately, using charge sharing between adjacent pixels in the strong magnetic field of CMS.

The bulk of the sensor is n-material and the implants are n^+. The negative bias voltage is applied to the backside and hence the readout signal is generated by electrons.

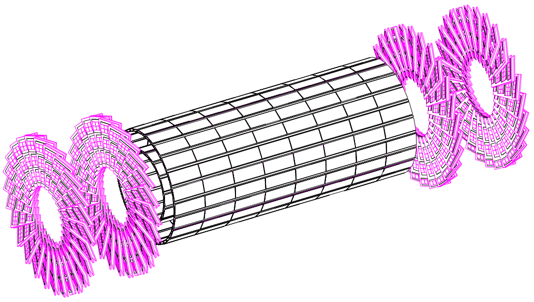

Figure 10.3: *Perspective view of the CMS pixel detector.*

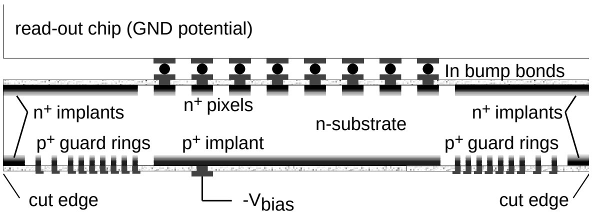

Figure 10.4: *Design of a sensor plate connected to the readout chip. The bias voltage is applied to the backside.*

Table 10.1: *Number of channels and rates at the design luminosity of* $10^{34} cm^{-2} s^{-1}$.

	Barrel (r)			End cap (z)	
Layer	4 cm	7 cm	11 cm	33 cm	47 cm
Number of chips	2340	2840	5888	1080	1080
Number of pixels	6.35×10^6	10.6×10^6	16.2×10^6	3.0×10^6	3.0×10^6
Area	0.15 m^2	0.25 m^2	0.38 m^2	0.07m^2	0.07 m^2
Pixel hit rate	24.0 kHz	10.3 kHz	6.9 kHz	lower	

The depletion layer grows from the backside (p^+ layer) and reaches the n^+ implants at full depletion (typically 150 V and up to several 100 V for irradiated devices). However, after irradiation, type inversion occurs (due to displacements of atoms in the lattice) and hence the depletion layer grows from the n^+ side. The guard rings ensure a smooth decrease of the bias potential over the edge so that the high field region does not reach the n^+ side which is at ground potential with the readout chip. For n^+ implants in n-material the pixels have to be isolated from one another. This is usually done with one or several narrow p^+-rings around each pixel (the so-called p-stop rings). To avoid excessive charging of a floating pixel (one with poor indium connection to the chip), leading to local discharges and momentary failures of whole pixel clusters, the resistance between pixels should remain finite. A narrow resistive path between the pixels would prevent the pixels from charging up. This is accomplished by small openings in the p-rings which lead to atoll-like structures. Figure 10.5 shows our favorite design for the elementary sensor cell.

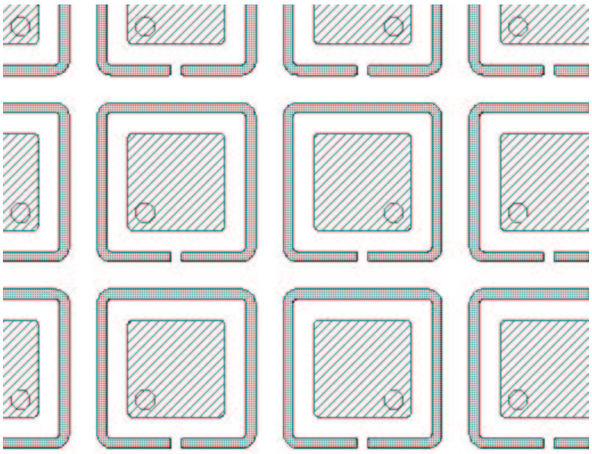

Figure 10.5: *Sensor design with one p-stop ring surrounding the pixels. The sizes of the* n^+*-implants and the spacings are typically 75* μm *and 10* μm*, respectively.*

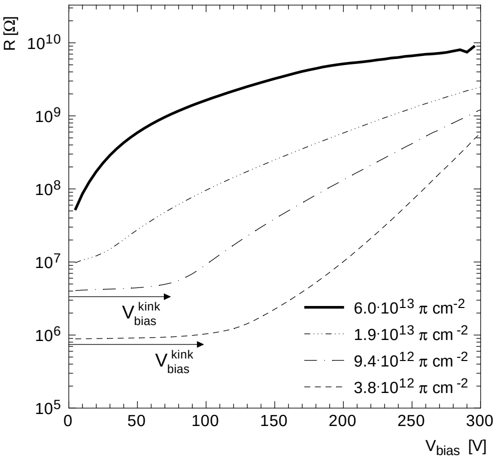

Figure 10.6: *Interpixel resistance as a function of bias voltage, for various particle fluxes. The kink in the bias voltage vanishes when type inversion occurs.*

During 2001 we performed many tests on the sensor designs that were submitted to SINTEF (Oslo) and CSEM (Neuchâtel) [5]. A sample of 16 layouts, including various p-stop ring geometries and guard rings, were produced on 24 wafers with different resistivities. We inspected the planarity of the delivered devices, performed leakage current and $C-V$ measurements with a probe station, and determined from the depletion voltage the doping concentration (donor concentration in the bulk, $2\times\ 10^{12}$ cm^{-3}). In the implants the concentration was determined to be $n^+ = 10^{18}$ cm^{-3}. The interpixel resistance was found to be typically a few MΩ, depending on the p-stop ring design.

Some of the devices were then irradiated with protons at the ROSE facility at CERN, and with pions at PSI. We determined the radiation dose at which type inversion occurs: after type inversion there is no flat interpixel resistance regime as a function of bias voltage, as there is no undepleted zone between the implants (the depletion layer grows from the n^+ side). For CSEM (SINTEF) devices type inversion occurs at a dose of 2.1×10^{13} (3.6×10^{13}) hadrons cm^{-2} (the expected radiation dose is 6×10^{14} after 10 years of LHC operation). The resistance is shown in Fig.10.6 for several irradiation doses. One finds that the interpixel resistance rises dramatically with dose, reaching several GΩ at full irradiation. Nonetheless, a beam test with an irradiated bump-bonded sensor showed a satisfactory behaviour without stochastic discharges in spite of this very high resistance.

We also measured the pixel capacitance (25.8 ± 1.8 fF, in good agreement with calculations) between a pixel and its neighbours and the backplane, by connecting many pixels in parallel. This result is very important for readout noise considerations.

From these and other R &D investigations [5] we conclude that the pixel detector envisaged in the proposal [4] is feasible. In 2002 we will investigate oxygen enriched sensors, for which the radiation hardness is increased due to the reduced acceptor concentration in n-type silicon [6].

10.3 Tests of the readout chip

Figure 10.7 explains the operation of the pixel readout chip (developed at PSI). The pixels are grouped in double columns, with a common bus to a double column periphery which controls the chip. The chips are produced in the radiation hard DMILL SOI (silicon on insulator) technology. Each pixel has its pixel unit cell (PUC), which consists of an analog and a digital block. It is equipped with a comparator allowing individually adjustable thresholds. Whenever a PUC detects a signal above threshold it stores the analog signal in a capacitor and notifies the double column periphery, which copies a time stamp into memory and requests a readout. A readout token is then sent through the chip and all double columns with hits are read out.

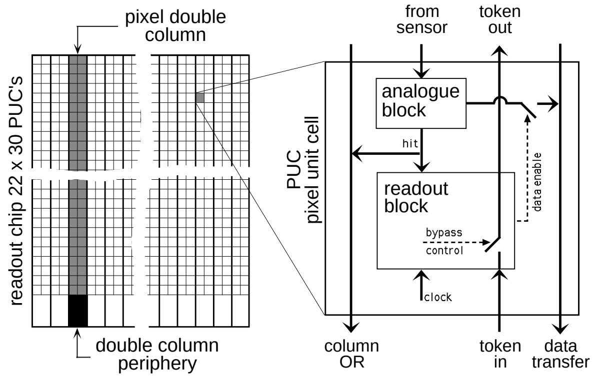

Figure 10.7: *Schematic of the PSI34 readout chip.*

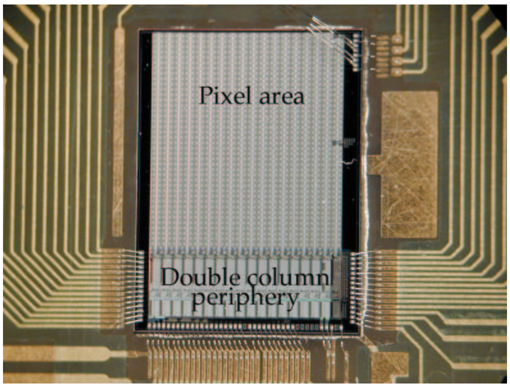

Figure 10.8: *Readout chip (version DM-PSI41) bonded to a test printed circuit board.*

Each pixel is hit at an average rate of 10 kHz, and the information (address and collected charge) has to be stored for 3.2 ms in the front end part of the pixel readout electronics (Fig.10.8), until it is read out or discarded by the external readout electronics. The front end part of the electronics consists of the following parts: readout chip (ROC), line drivers, $\mathrm{I}^2\mathrm{C}$

interface for controlling, token bit manager chip (TBM). Each readout chip reads out 2756 pixels (53 columns × 52 rows), and 16 readout chips are controlled by one token bit manager chip. The read out chip contains analog preamplifiers, shapers and discriminators, column periphery, readout buffers/amplifiers.

The analog preamplifier is made of two integrating amplifiers and one differentiating stage. Last year a preliminary version of the readout chip (DM-PSI41) was tested in our lab. Several parameters were optimised to get acceptable gain, peaking time and power dissipation. The minimum power consumption was determined as a function of gain and peaking time by varying the supply voltages to the amplifiers. It is typically 25 μW per channel.

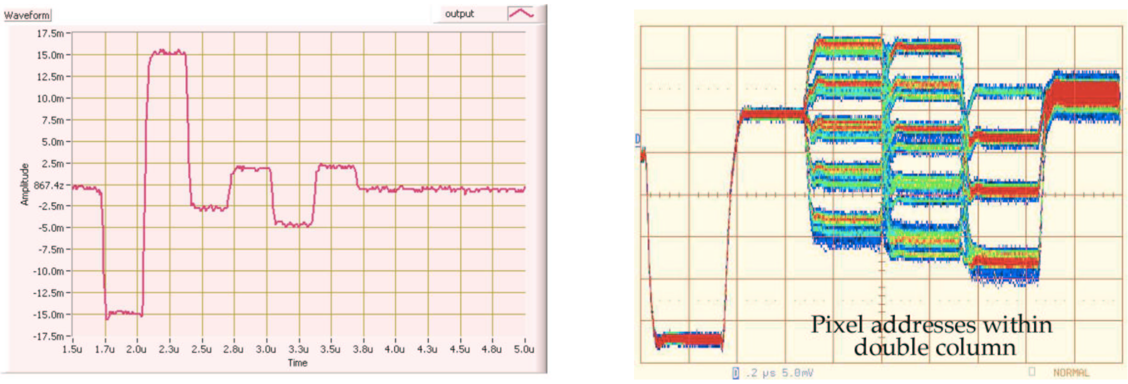

Figure 10.9: *Output signals from the readout chip for a single hit pixel (left) and for 80 superimposed signals from different pixels of the same double column (right). The six time bins encode the address and the charge collected by the pixel (see text).*

We also tested the digital part of the readout chip DM-PSI41 with a digital pattern generator DG2020 and a PCI digital I/O card. Because of the expected huge data rates at LHC (32 Gb/s), a 5-level logic is used instead of binary logic. For each hit pixel, the readout chip produces a signal (shown in Fig.10.9), which is divided into six bins. The first two bins encode the double column address and the next three encode the pixel address within the double column. With five levels a total of $5^5 = 3125$ pixel addresses can be encoded by one readout chip. The sixth bin represents the analog signal from the pixel.

10.4 Simulation and reconstruction software

The Zürich group has taken major responsibilities in the development of the reconstruction software. Charged particles usually leave between 8 and 15 hits in the tracker (pixel and silicon detectors), depending on rapidity. The challenge is to reliably find tracks in a reasonable amount of time in a high rate environment (see the typical event of Fig.10.1 above), where low luminosity events will feature around 5000 hits and high luminosity events ten times more. Combinatorial problems can thus be severe.

Figure 10.10 shows the new cms121 layout of the silicon tracker. We discovered that the transverse momentum resolution of high-p_t single muon tracks deteriorated significantly (Fig.10.11) when the microstrip gas chambers (cms118 layout) were replaced by the current all-silicon configuration. We could attribute this deterioration to the removal of one layer, reducing the average track length by 10 cm, to the gap between the outer barrel and the endcap detectors, and to a degradation of the resolution in the last rings of the disks.

A possible improvement is to reduce the average pitch of the sensors in the 7th (last) ring of the endcap disks from 156 to 104 μm. The effect on mass resolution was studied for the

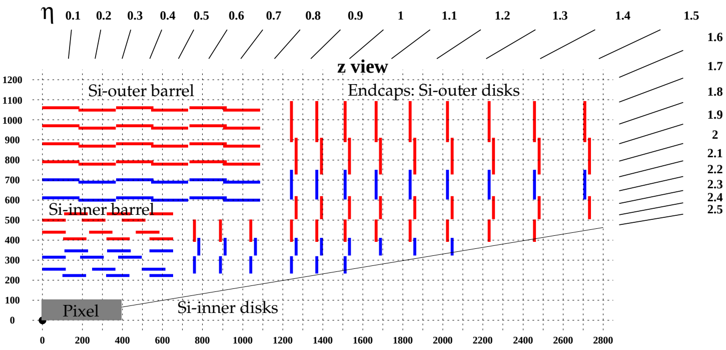

Figure 10.10: *The current cms121 all-silicon layout of the tracker; red, single-sided, blue double-sided readout. The parameter η denotes the pseudorapidity.*

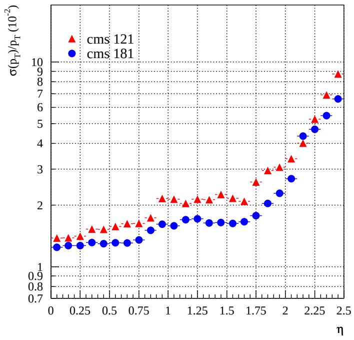

Figure 10.11: *p_t-Resolution for muons with p_t=100 GeV/c versus pseudorapidity η for the cms118 and cms121 configurations.*

decay $H \rightarrow Z^0 Z^0 \rightarrow 2(\mu^+\mu^-)$. No improvement was observed since muons from Higgs decay are emitted with relatively low transverse momenta (below 50 GeV/c), where the resolution is dominated by multiple scattering. On the other hand, improvements on the mass resolution are expected for higher mass objects ($\sim$ 400 GeV) for which the decay momentum spectrum is harder. These states are, however, not expected to be narrow.

We also studied the effect of an increase of the pitch of the sensors of the first two Outer Barrel layers from 122 to 133 μm which would lower the number of readout chips by 2160 units. In this case b and τ jets were used in the simulation. The modification which affects only hits in the middle of the tracks turned out to have little effect on the momentum resolution. Since the track reconstruction efficiency remained essentially unchanged the pitch will be increased in these layers to reduce costs.

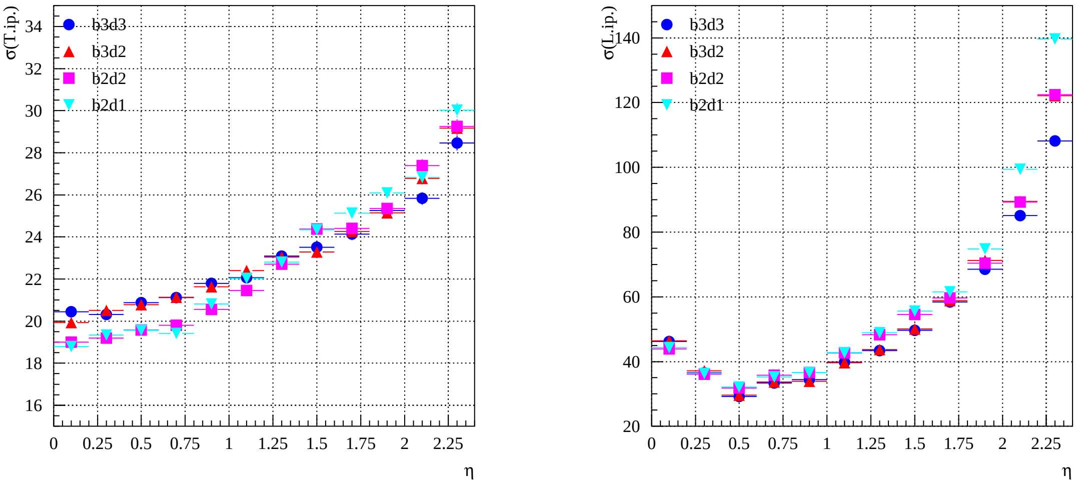

Figure 10.12: *Resolution of the transverse (left) and longitudinal (right) impact parameter (in μm) as a function of the pseudo-rapidity η for different configurations and 10 GeV/c muons.*

We studied several alternatives for the number of pixel layers which were discussed at a workshop in December 2001. The resolution on transverse momentum depends slightly on the radius of the innermost layer, as it is mostly determined by the total length of the track. The resolution on the azimuthal angle ϕ in the barrel improves slightly with the number of layers, but the resolution on the polar angle improves significantly, both in the barrel and in the endcaps. At high momentum the resolution on the transverse impact parameter (Fig. 10.12, left) improves with the number of barrel layers, but shows no significant dependence on the number of disks. However, at low momentum, the resolution is best with two barrel layers, due to the reduction of material thickness. The resolution on the longitudinal impact parameter (Fig. 10.12, right) shows little dependence on the number of barrel layers but improves dramatically with the number of endcap disks. No dramatic change was observed, the layout with the largest number of layers offering the best performance. The pixel system will therefore consist of three barrel layers and two pairs of endcap disks.

We also studied the detection efficiency as a function of LHC bunch length. At injection the length of the longitudinal beam overlap is about 11 cm (FWHM). From experience with $\bar{p}p$ collisions at the SPS collider this length will increase to 18 cm (FWHM) after 10 hours of coasting beams. To estimate the coverage in $\eta - \phi$ of each layer as a function of vertex position, muons with a transverse momentum of 100 GeV/c were generated with a uniform $\eta - \phi$ distribution and a vertex z-coordinate between between -30 and 30 cm. The coverage of the barrel pixel layers is fortunately not sensitive to the vertex position. The inefficiency is 2.9% in each layer (Fig.10.13, left), resulting mainly from the longitudinal gaps between the pixel modules, see Fig.10.13 (right). The coverage of the forward disks is, as expected, strongly dependent on the vertex position, and the total inefficiency is about 2%, mainly due to the radial gaps between the pixel modules.

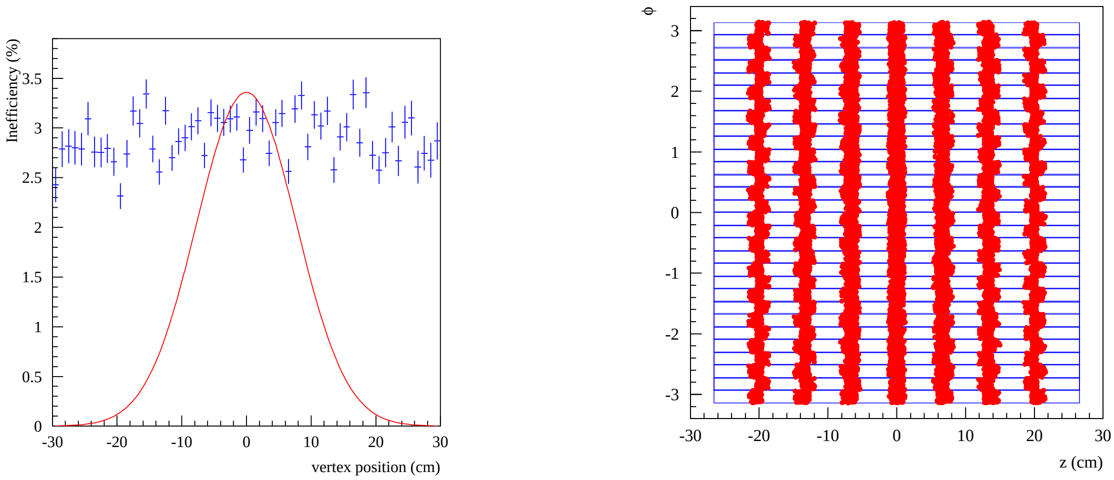

Figure 10.13: *Left: inefficiency as a function of vertex position for the second barrel pixel layer (crosses) and expected distribution of collision points after 10 hours of coasting beams (curve); right:* $\phi - z$ *view of the detector modules showing the missing hits in the second barrel pixel layer.*

In 2002 we will complete the optimisations of the tracker geometry and tackle the vertex reconstruction. Our aim is to study and implement robust secondary vertex fit procedures, which are not sensitive to tracks that have a small probability to emerge from the secondary vertex.

References

[1] V. Dubacher, *Test of a Silicon Pixel Detector with 50 GeV Pions*, Universität Zürich (1996); R. Kaufmann, *Performance of a Silicon Pixel Detector in a Magnetic Field*, Universität Zürich (1997); M. Glättli, *Untersuchung von Silizium-Pixeldetektoren mit einem Silizium-Mikrostreifen-Strahlteleskop*, Universität Zürich (1998).

[2] G. Bolla *et al.*, Nucl. Instr. Meth. in Phys. Research **A** 461 (2001) 182.

[3] B. Henrich, R. Kaufmann, Nucl. Instr. Meth. in Phys. Research **A** 304 (2002) 304.

[4] The Tracker Project, Technical Design Report, CERN LHCC 98-6, CMS TDR 5 (1998).

[5] R. Kaufmann, PhD thesis, Universität Zürich (2001).

[6] M. Moll, E. Fretwurst, G. Lindström, Nucl. Instr. Meth. in Phys, Res. **A** 439 (2000) 282.